Article

Complete Crystal Structures and Elastic Properties of the Uranyl Minerals Johannite, Pseudojohannite and Derriksite

Francisco Colmenero [1,*], **Jakub Plášil** [2] **and Jiří Sejkora** [3]

1   Departamento de Química-Física, Facultad de Ciencias Químicas, Universidad Complutense de Madrid, 28040 Madrid, Spain
2   Institute of Physics of the CAS, v.v.i., Na Slovance 2, 182 21 Praha, Czech Republic
3   Mineralogicko-Petrologické Oddělení, Národní Muzeum, Cirkusová 1740, 193 00 Praha, Czech Republic
*   Correspondence: francolm@ucm.es

Abstract: Due to the high solubility of uranyl sulfate and selenite minerals, the investigation involving the determination of the crystal structures and physical properties of these minerals is essential in actinide environmental chemistry for the simulation of uranium migration from uraninite deposits and nuclear waste repositories. However, the determination of the complete crystal structures of the uranyl sulfate minerals johannite ($Cu(UO_2)_2(SO_4)_2(OH)_2 \cdot 8H_2O$) and pseudojohannite ($Cu_3(UO_2)_4(SO_4)_2O_4(OH)_2 \cdot 12H_2O$) and the uranyl selenite mineral derriksite ($Cu_4[((UO_2)(SeO_3)_2(OH)_6])$) has not been feasible so far. In this work, the crystal structures of these minerals, including the positions of the hydrogen atoms, are determined using first principles solid-state methods based on periodic density functional theory using plane wave basis sets and pseudopotentials. The lattice parameters and associated geometrical variables as well as the corresponding X-ray diffraction patterns derived from the computed crystal structures are in excellent agreement with their experimental counterparts, derived from the corresponding experimental structures lacking the hydrogen atom positions. The complete crystal structure of derriksite is also determined by refinement from X-ray diffraction data, the resulting structure being consistent with the computed one. The knowledge of the positions of H atoms is of fundamental importance not only because they define the corresponding hydrogen bond networks holding together the atoms in the structures, but also because it allows for the efficient, inexpensive and safe determination of the physical properties using first principles methods. This feature is particularly important in the case of uranium-containing minerals due to their radiotoxicity, complicating the handling of the samples and experimental measurements. In this work, from the computed crystal structures, the elasticity tensors of these minerals are computed using the finite displacement method and a rich set of elastic properties including the bulk, Young's and shear moduli, the Poisson's ratio, ductility, anisotropy and hardness indices and bulk modulus derivatives with respect to pressure derivatives are determined.

Keywords: uranyl sulfate minerals; uranyl selenite minerals; crystal structures; X-ray diffraction; mechanical properties; periodic density functional theory

1. Introduction

Investigations on the chemistry of aqueous uranyl sulfate ions under hydrothermal conditions, powered by the nuclear industry, has been mainly driven by the Generation IV nuclear reactor program [1,2]. However, the research involving the determination of the crystalline structures and physical properties of uranyl sulfate and uranyl selenite minerals is less developed despite its crucial role in actinide environmental chemistry for the simulation of the uranium migration from uraninite deposits and nuclear waste repositories due to their high solubility in aqueous solutions. While uranyl selenite minerals are less abundant, these minerals are also very interesting from radiochemical and geochemical points of view. Fission products contain 53 g per ton [3] of the ^{79}Se isotope, having

a half-life of 1.1×10^6 years [4] three years after nuclear fuel irradiation. Therefore, understanding the formation processes of natural and synthetic selenites is important for the processing of spent nuclear fuel. Following a previous study on the structure and physical properties of the uranyl sulfate oxyhydroxide tetradecahydrate mineral uranopilite [5], the hydrated copper uranyl sulfate minerals johannite [6–20] $(Cu(UO_2)_2(SO_4)_2(OH)_2 \cdot 8H_2O)$ and pseudojohannite [21–25] $(Cu_3(UO_2)_4(SO_4)_2O_4(OH)_2 \cdot 12H_2O)$ and the copper uranyl selenite hydroxide mineral derriksite $(Cu_4[((UO_2)(SeO_3)_2(OH)_6)$ [26–31] were selected for this study. These minerals, whose complete crystal structures are unknown, are well-known secondary minerals, important for studying the oxidative dissolution processes occurring in spent nuclear fuel repositories and uranium deposits [32–34]. The study of these minerals is also important in environmental investigations of acid mine drainage, since they are also found after the oxidative dissolution processes of sulfide and selenide minerals, commonly found in uranium mineral deposits, occurring when they are exposed to air, water, and microorganisms [35–38]. These processes result in the formation of solutions with low pH, containing high concentrations of metals and toxic elements which are extremely harmful for flora and fauna. The term "complete crystal structures" means that the unit cell parameters and fractional coordinates of all atoms in the unit cell of these minerals are fully specified. The previous crystal structures lack the positions of the hydrogen atoms due to the insufficient quality of the X-ray diffraction patterns. Without these positions, it is impossible to describe the forces holding together the atoms in the corresponding crystal structures because hydrogen bonding is one of the most important bonding forces in these minerals.

The uranyl sulfate mineral group displays an extremely large structural and compositional variety and contains more than thirty different mineral species [32]. Mineral uranopilite [5] belongs to uranyl sulfate Group I, not containing metallic cations. This mineral is of primary importance, since it one of the earliest uranyl sulfate minerals appearing in the paragenetic sequence of uranyl-containing minerals appearing after the corrosion of uraninite ore deposits when uraninite is exposed to sulfur-rich solutions with low pH. Johannite belongs to Group II, appearing rapidly where uraninite or Group I minerals are associated with primary copper sulfide minerals (as chalcopyrite and tennantite). Finally, pseudojohannite, despite its name, is structurally unrelated to johannite [23], and belongs to the zippeite group (III), whose component minerals are later in the paragenetic sequence. Selenite mineral group, while important [30], is much less numerous and contains only nine minerals, the most important ones, together with derriksite, being guilleminite, demesmaekerite, and marthozite [30].

Mineral johannite has been known since the earliest years of 19th century and was first described by John in 1821 [6] under the name "uranvitriol", and later named by Wilhelm Karl Ritter von Haidinger 1830 [7,8]. Its name was coined after Archduke John of Austria (1782–1859), the founder of the Landesmuseum Joanneum (Styria, Austria) and has long been investigated [6–20]. Its chemical composition was first established in 1935 by Nováček [10], although the number of water molecules per unit cell was not correct. The correct composition was later inferred by Mereiter [15,16] (eight water molecules and two hydroxyl ions) and confirmed on natural and synthetic johannite [18–20]. Its symmetry was shown to be triclinic by Hurlbut [12] and later by Donnay [13], and its structure was finally described by Mereiter [15,16]. However, this important mineral is highly hydrated and, unfortunately, the positions of the hydrogens in its structure are not known. It is a widely distributed mineral, the main localities including Argentina, Czech Republic, Gabon, Germany, Greece, France, Italy, Switzerland, United Kingdom and the United States. The type locality is "Elias Mine" in Jáchymov (Czech Republic). Pseudojohannite, however, was first described at the end of the 20th century by Ondruš et al. in 1997 and later in 2003 [21,22] from samples from Jáchymov ore district (St. Joachimsthal, Western Bohemia, Czech Republic). These authors showed it to be triclinic. Its name was coined on the basis of the common elemental composition with johannite. However, based on the characteristic U:S ratio of 2:1, Brugger et al. [23] showed it to belong to the zippeite mineral group from a

synchrotron powder diffraction study without full structure determination. This feature was confirmed by Plášil et al. [24,25], which reported its final formula and studied the structure from a sample from Widowmaker mine, White Canyon, San Juan County, Utah, USA, using single-crystal X-ray diffraction. However, the data quality was not sufficient to reveal the hydrogen positions. Pseudojohannite is much less widely distributed than johannite, with the type locality being Jáchymov (Czech Republic). Finally, derriksite has low abundance, although it has been found in multiple localities in Congo, USA, France, Switzerland and Spain [31]. Derriksite was first found in the oxidized zone of the of Musonoi (Katanga, Democratic Republic of Congo) copper–cobalt deposit and named after Jean-Marie François Joseph Derriks, a Belgian geologist and administrator of UMHK (Union Minière du Haut-Katanga). The crystal structure of derriksite, lacking the positions of hydrogens, was reported by Ginderow and Cesbron in 1984 [27]. Several studies concerning this mineral and the uranyl selenite mineral group have been published [26–31].

In this work, the crystal structures of the minerals johannite, pseudojohannite and derriksite, including the positions of the hydrogen atoms, are determined using first principles theoretical methods based on periodic density functional theory (DFT). The complete crystal structure of derriksite is also determined by refinement from X-ray diffraction data. The knowledge of the positions of the hydrogen atoms defining the corresponding hydrogen bond networks holding together the atoms in the structures, is important because it allows for the efficient and safe determination of the physical properties of these minerals using first principles methods [5,39–42]. This feature is particularly important in the case of uranium containing minerals due to their radiotoxicity, complicating the handling and experimental measurements. In this work, from the computed crystal structures, the elasticity tensors of these minerals are computed using the finite displacement method and a rich set of mechanical properties including the bulk, Young's and shear moduli, the Poisson's ratio, ductility, hardness and anisotropy indices and bulk modulus pressure derivatives are determined.

2. Materials and Methods

2.1. Experimental

A derriksite natural crystal from Musonoi (Democratic Republic of the Congo) was studied by means of single-crystal X-ray diffraction. A dark green prismatic crystal (approximately 1 mm in length) was used for room temperature X-ray diffraction data collection with a Rigaku SuperNova single-crystal diffractometer using MoKα radiation from a microfocus X-ray tube collimated and monochromatized by mirror-optics and detected by an Atlas S2 CCD detector). The crystal structure determination led, in accordance with previous structure refinements [27], to the results that derriksite is orthorhombic, space group $Pn2_1m$ (no. 31) with a = 5.9655(2) Å, b = 5.5755(2) c = 19.0960(5) Å, $\alpha = \beta = \gamma$ = 90.0, V = 635.15(4) Å^3 (Z = 2). The integration of X-ray diffraction data, including polarization, background and Lorentz and absorption corrections, was conducted with the CrysAlis RED proGram [43]. The structure of derriksite was solved by the Intrinsic Phasing method using the SHELXT computer proGram [44]. The structure was then refined employing Jana2006 software with the full-matrix least-squares refinement based on F^2 [45]. The position of all atoms except hydrogens were revealed in the structure solution. The positions of hydrogen atoms were ascertained from the difference-Fourier maps. The H atoms were refined using a mix of soft constraints on O–H distances and with the atomic displacement parameter, U_{eq}, of each H set to 1.2 times that of the donor O atom. The crystallographic and refinement data, together with the final fractional coordinates and anisotropic displacement parameters in the crystal structure of derriksite are given in Tables S1–S3 of the Supplementary Material (SM). The final structure is also given in the SM as a file of the CIF (Crystallographic Information File) type. It must be noted that, in the current setting, derriksite has the space group $Pmn2_1$.

2.2. First Principles Solid-State Methods

The crystal structures and mechanical properties of johannite, pseudojohannite and derriksite were modeled using first principles solid-state methods based on Density Functional Theory (DFT) using basis sets composed of plane waves and pseudopotential functions to describe the inner electrons [46]. All the calculations were performed using the Cambridge Serial Total Energy ProGram (CASTEP) computer code [47] interfaced with the Materials Studio proGram package [48]. The Perdew–Becke–Ernzerhof (PBE) energy-density functional [49] complemented with D2 Grimme empirical correction [50] was used. All the computational works were performed using standard norm-conserving pseudopotentials [51] for all atoms, except for uranium. In this case, a high-quality new scalar-relativistic norm conserving pseudopotentials developed in a previous work [52] was employed. The material data and calculation parameters of the three minerals studied are collected in Table S4 of the SM. The BFGS (Broyden–Fletcher–Goldfarb–Shanno) method [53] was employed to optimize completely their crystal structures, that is, all the atomic positions and unit cell parameters, were determined. The structure optimizations were performed using the experimental structures reported by Mereiter [16], Plášil et al. [24] and Ginderow and Cesbron [27] for johannite, pseudojohannite and derriksite, respectively, as starting point. Since these structures, lack the hydrogen atom positions, they were supplemented by initial values of these positions using a simple procedure. The closest oxygen atoms to each water molecule or hydroxyl oxygen atom in the crystal structure were found. Then, two hydrogen atoms were placed along the lines linking the water oxygen atoms and two near oxygen atoms with the condition that the geometry of a water molecule is approximately satisfied. For the hydroxyl oxygen atoms, only one hydrogen atom must be introduced. The hydrogen atoms were put at a distance from the water or hydroxyl oxygen atoms of about 1.1 Å. These distances are only used to provide reasonable initial position of the H atoms which are later submitted to unconstrained full optimization. BFGS method was then used to fully optimize all the possible structures resulting from the different initial positions of the hydrogen atoms. These optimizations yielded several final structures. The positiveness of the energy hessian matrix for these structures was checked. All structures except one were discarded using energy criteria. All geometry optimizations were performed using stringent convergence tolerances. The thresholds in the variation of the total energy, maximum atomic force, maximum atomic displacement, and maximum stress were of 2.5×10^{-6} eV/atom, 0.005 eV/Å, 2.5×10^{-4} Å and 0.0025 GPa, respectively. The X-ray diffraction patterns [54] of the minerals under study were derived from the experimental and computed crystal structures using CuKα radiation (λ = 1.540598 Å) using the REFLEX software included in Materials Studio program suite [48].

The elements of the stiffness matrix [55], the so-called elastic constants, needed to assess the mechanical stability of their crystal structures and to evaluate the elastic properties of the minerals considered, were determined using the finite deformation method (FDM) [56]. In this method, the individual elastic constants are determined from the stress tensors resulting from the response of the material to finite programmed symmetry-adapted strains [56] using stress-strain relationships. This technique has been successfully employed to describe the elastic properties many solid materials, such us uranium-containing compounds [5,39,41,42], organic crystals [57,58] and metal-organic compounds [59–61]. The reliability of the computed elastic properties has been established recently by the experimental confirmation of the negative area compressibility effect in silver oxalate [60], which was predicted using first principles methods [59]. The ElAM computer program [62] was employed to generate 3D representations of the elastic properties as a function of the orientation of the applied strain. The structures of the uranyl minerals studied in this work were fully optimized under the effect of fifteen different external isotropic pressures in the range going from −1.0 to 9.0 GPa. The pressure-volume (PV) data obtained were then fitted to a Birch-Murnaghan equation of state of 4th order (4-BM-EOS) [63]. From the values of the fit parameters, the derivatives of the bulk-modulus with respect to pressure were derived. Angel's EOSFIT 5.2 software [64,65] was employed to fit the PV-data to the

selected equation of state. The BFGS method was also used for performing the full structure optimizations under pressure.

3. Results and Discussion

3.1. Crystal Structures

3.1.1. Johannite

The computed crystal structure of johannite mineral is displayed in Figure 1. Uranium in johannite displays pentagonal bipyramidal, $UO_2[O_3(OH)_2]$ coordination. Uranyl polyhedra are composed of a nearly linear uranyl ion and five equatorial ligands $[O_3(OH)_2]$. Thus, hydroxyl ions are placed in equatorial positions. Likewise, the sulfur atom displays tetrahedral coordination, SO_4, and the copper exhibits octahedral coordination, $CuO_2[(OH_2)_4]$. As can be observed in Figure 1, the structure of johannite is layered (Figure 1A), with the interlayer space between the sheets being occupied by copper polyhedra. Johannite sheets (Figure 1B) consist of pairs of pentagonal bipyramids sharing an equatorial edge, which are linked through the vertices of SO_4 tetrahedra to form uranyl sulfate layers with a composition $[(UO_2)(OH)_2(SO_4)]^{4-}$. Copper ions are linked up and down with the uranyl sulfate layers through the oxygen ions in the apical positions. The layers in johannite are obtained from the phosphuranylite anion topology by populating each pentagon with a uranyl ion and each triangle of the anion topology with the face of a SO_4 tetrahedron, the hexagons being vacant in johannite [32].
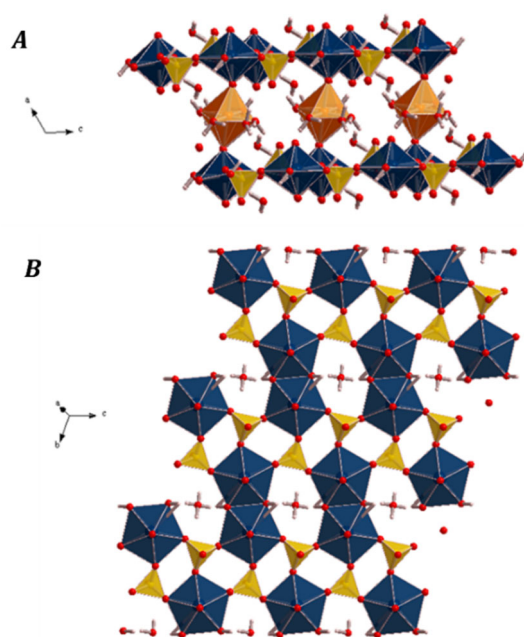

Figure 1. Views of the crystal structure of johannite mineral: (**A**) view of the unit cell from the [0 1 0] direction; (**B**) view of a johannite uranyl sulfate sheet. Color code: Cu—orange; U—blue; S—yellow; O—red; H—white.

The computed and experimental unit cell parameters of johannite are presented in Table 1. As can be observed, these parameters are well reproduced, theoretically, with the unit cell volume being underestimated by 2.6%. As can be noticed in the first row of Table 1, in the present case, the PBE functional, without dispersion corrections, overestimates the unit cell volume by 4.6%. Thus, dispersion corrections improve the results significantly. The calculated interatomic distances are compared with their experimental counterparts [16] in Table S5 of the SM. The $U - O$ distances are well reproduced, with the differences in the average $U - O$ apical and equatorial distances being about 0.02 Å. The $Cu - O$ distances are also satisfactorily obtained, with the differences being at most 0.07 Å. Finally, the differences in the interatomic distances in the sulfate tetrahedra are reproduced within 0.02 Å.

From the computed and experimental crystal structures of johannite, the X-ray diffraction pattern of johannite was derived. The resulting patterns, shown in Figure 2, are consistent. A detailed comparison of the positions of the most intense reflections in the experimental and computed patterns is provided in Table S8 of the Supplementary Materials.

Table 1. Calculated lattice parameters of johannite, pseudojohannite and derriksite minerals.

| Parameter	a (Å)	b (Å)	c (Å)	α (deg)	β (deg)	γ (deg)	Vol. (Å³)	ρ (g/cm³)
				Johannite				
PBE	9.4683	9.6198	6.8980	110.80	111.46	102.37	502.0302	3.220
DFT-D2	8.9602	9.4402	6.7871	109.27	110.56	103.14	467.5905	3.458
Exp. [16]	8.9030	9.4990	6.8120	109.87	112.01	100.40	480.1969	3.367
				Pseudojohannite				
PBE	8.6934	9.0300	10.1807	74.56	71.74	75.88	720.2325	4.097
DFT-D2	8.6160	8.9516	10.0226	76.61	71.09	75.86	699.2791	4.220
Exp. [24]	8.6744	8.8692	10.0090	72.11	70.54	76.04	682.6059	4.323
				Derriksite				
PBE	6.1425	5.9530	5.9530	90.00	90.00	90.00	697.2246	5.480
DFT-D2	6.1180	5.8027	18.8629	90.00	90.00	90.00	669.6411	5.706
Exp. (This work)	5.9655	5.5755	19.0960	90.00	90.00	90.00	635.1452	6.016
Exp. [27]	5.570	5.965	19.088	90.00	90.00	90.00	635.15(2)	6.025
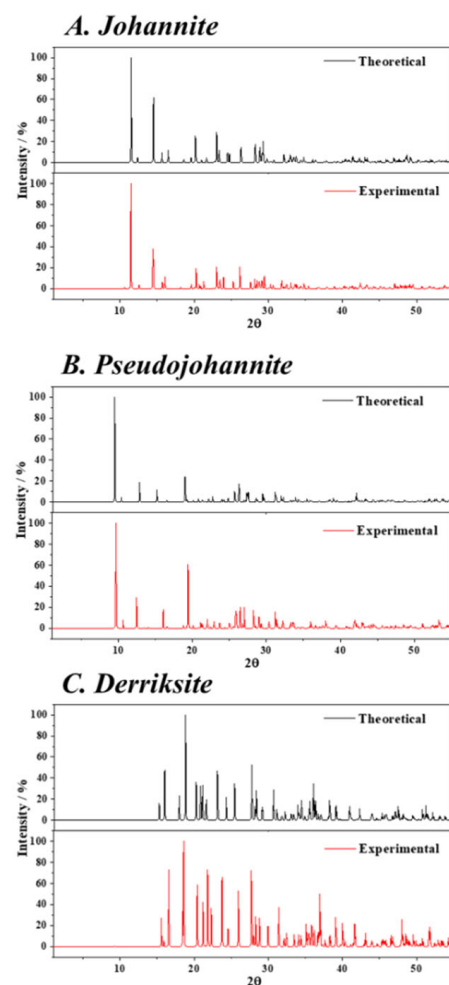
Figure 2. X-ray diffraction patterns of johannite, pseudojohannite and derriksite derived from experimental [16,24,27] and theoretical crystal structures.

Hydrogen Bonding Network

There are four non-equivalent water molecules in the unit cell of johannite—W8, W9, W10 and W11—and one hydroxyl ion, OH3. W8 and W9 form part of the coordination environment of the copper atom and W10 and W11 are free water molecules. OH3 enters in the coordination sphere of U atom in its equatorial structure. The hydrogen bond structure derived from the computations is shown in Figure 3. As can be observed in Table 2, there are nine non-equivalent hydrogen bonds in the structure of johannite. In the first hydrogen bond, OW8–H8WB· · ·OW10, the donor oxygen atom, OW8, is from water molecule W8 (belonging to Cu coordination structure) and the acceptor oxygen atom, OW10, is from a free water molecule, W10. The next H bond is also from W8, and the acceptor O atom, O7, is from a S tetrahedron. The hydrogen bonds from OW9 are similar, one links W9 with the free water molecule W1 and the other W9 with O7 from an S tetrahedron. The hydrogen bonds arising from the free water molecule OW10 as hydrogen bond donor links W10 with the free water molecule W11 and W10 with an O atom (O1) of U coordination polyhedra. The free OW11 links W1 with OW9 from Cu coordination structure and the hydroxyl ion OH3 from U coordination structure. Finally, the hydroxyl OH3 links U polyhedra with a free water molecule. Thus, two hydrogen bonds link Cu octahedra with free water molecules, two hydrogen bonds link Cu octahedra with S tetrahedra, three hydrogen bonds link U bipyramids and free water molecules, one hydrogen bond links U bipyramids with Cu octahedra, and one hydrogen bond links two free water molecules. Consequently, the hydrogen bond structure in johannite servers to hold the full structure together by linking: (1) Cu octahedra, S tetrahedra and U bipyramids, (2) Cu octahedra with free water molecules and (3) Free water molecules with other free water molecules.
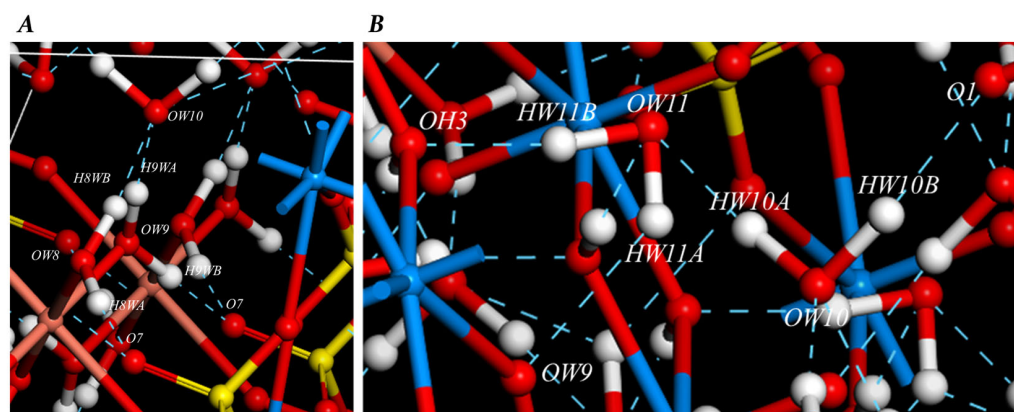

Figure 3. Hydrogen bonding structure in the crystal structure of johannite. (**A**) Hydrogen bonds donated by OW8 and OW9; (**B**) Hydrogen bonds donated by OW10 and OW11.

Table 2. Hydrogen bond parameters in johannite (distances are given in Å and angles in degrees).

Hydrogen bond (O1-H· · ·O2)	O1· · ·O2	H· · ·O2	α(O1-H· · ·O2)
OW-H· · ·O			
OW8-H8WB· · ·OW10	2.664	1.712	157.73
OW8-H8WA· · ·O7	2.700	1.721	167.48
OW9-H9WB· · ·O7	2.721	1.748	165.69
OW9-H9WA· · ·OW10	2.672	1.710	160.12
OW10-H10WA· · ·OW11	2.774	1.797	168.34
OW10-H10WB· · ·O1	2.794	1.810	177.88
OW11-HW11A· · ·OW9	2.734	2.258	139.47
OW11-HW11B· · ·OH3	3.164	1.868	166.67
OH3-H3· · ·OW11	2.734	1.738	174.00
OH-H· · ·O			
OH3-HO3· · ·OW11	2.734	1.738	174.00

3.1.2. Pseudojohannite

The computed crystal structure of pseudojohannite is shown in Figure 4. The unit cell contains two non-equivalent uranium atoms, two non-equivalent Cu atoms and one distinct S atom. Uranium atoms display pentagonal bipyramidal coordination, UO_7. The S atoms are tetrahedrally coordinated, SO_4. The coordination structure of the non-equivalent Cu atoms is shown in Figure 5. The non-equivalent Cu1 atoms display octahedral coordination, $Cu(OH_2)_6$, with four shorter equatorial bonds and two longer axial bonds (see Table S6), typical of Jahn–Teller effect in Cu(II) [66]. However, the Cu2 atoms are coordinated by five ligands only $(Cu(OH_2)_3(OH)_2)$, with one long and four shorter bonds leading to a square pyramidal coordination, also typical for the Jahn–Teller distortion in Cu(II) [66]. Pseudojohannite possesses a layered structure. The uranyl bipyramids form chains by sharing equatorial edges with the other two uranyl bipyramids, as shown in Figure 4. Adjacent uranyl bipyramid chains are then linked by sharing equatorial vertices with the sulfate tetrahedra to form sheets with a composition $[(UO_2)_4O_4(SO_4)_2]^{4-}$, typical of zippeite topology [32]. The interlayer space is occupied by Cu2 atom pyramids forming chains with composition $[Cu_3(OH)_2(H_2O)_{12}]^{4+}$ running parallel to [1 0 0], joined through the pyramid apices through corner-sharing with the Cu1 octahedra. The interlayer structure in pseudojohannite is described in detail in the work by Plášil [25].
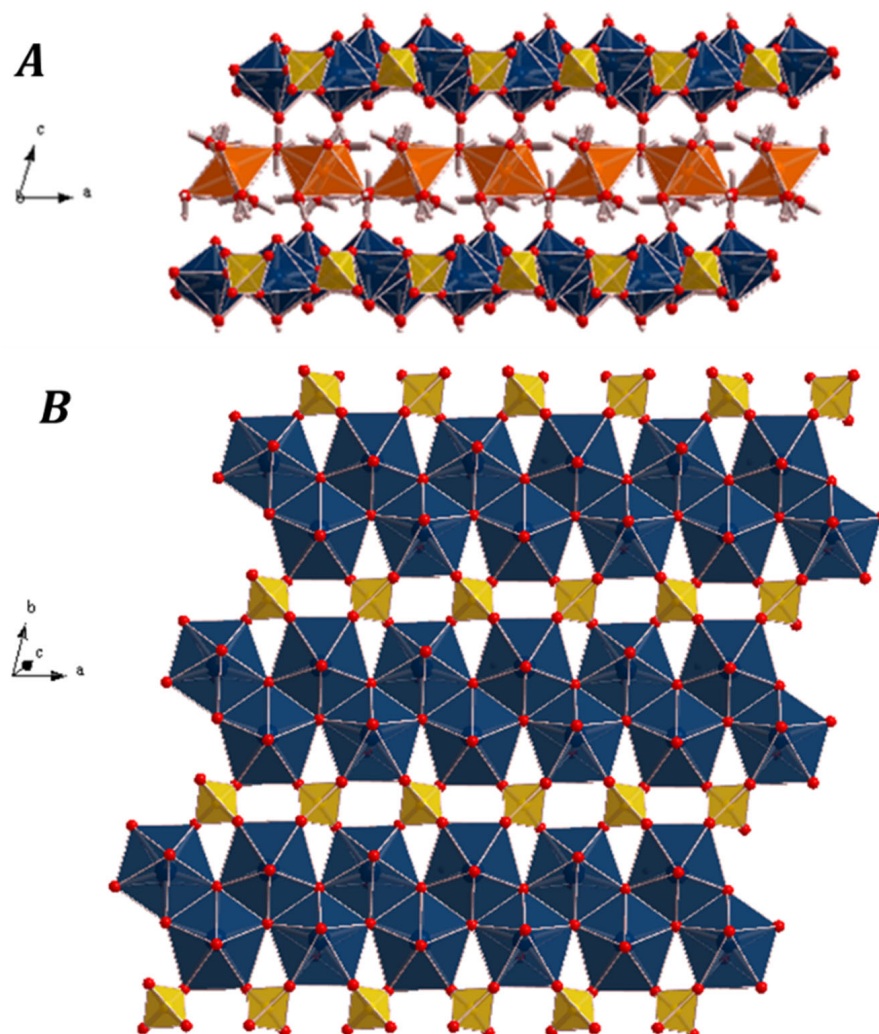

Figure 4. Views of the structure of pseudojohannite mineral: (**A**) view of the full unit cell from the [0 0 1] crystallographic direction; (**B**) view of a johannite uranyl sulfate sheet. Color code: Cu—orange; U—blue; S—yellow, O—red, H—white.
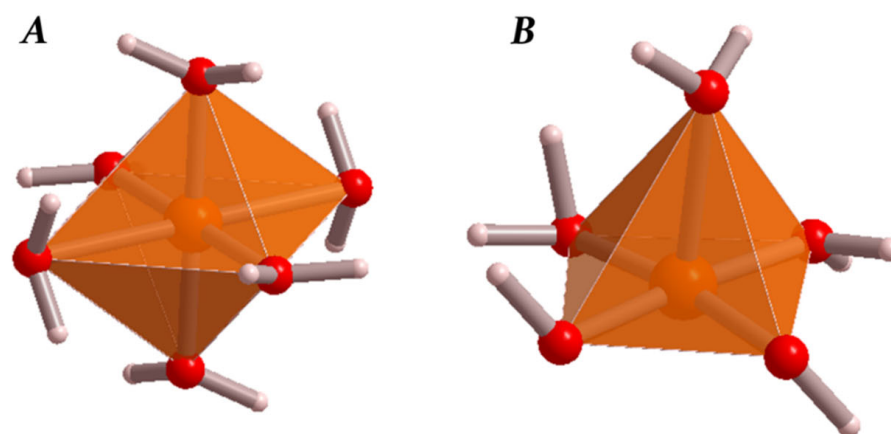
Figure 5. Structure of the Cu coordination polyhedra in mineral pseudojohannite: (**A**) Cu1 coordination polyhedron; (**B**) Cu_2 coordination polyhedron. Color code: Cu—orange; S—yellow; O—red; H—white.

The computed lattice parameters of pseudojohannite are given in Table 1. As in johannite, the unit cell parameters are also well reproduced. The unit cell volume is overestimated by 2.4%, and the PBE functional without dispersion corrections overestimates the unit cell volume by 5.5%. The calculated interatomic distances are contrasted with the experimental ones [24] in Table S6 of the SM. The average $U - O$ apical and equatorial interatomic lengths are reproduced within 0.02 Å. The $Cu - O$ and $Se - O$ distances are also satisfactorily obtained. The X-ray diffraction patterns of pseudojohannite derived from the computed and experimental crystal structures are shown in Figure 2, and, as can be observed are in good agreement. The positions of the most intense reflections in the computed and experimental patterns are compared in detail in Table S9 of the SM. The largest difference is observed in the [0 3 3] reflection, $\Delta = 0.01°$.

Hydrogen Bonding Network

There are six water molecules in the unit cell of pseudojohannite that are non-equivalent, W1, W4, W7, W9, W10, and W13, and one hydroxyl ion, OH3. W1, W4, and W9 form part of the coordination structure of the copper Cu1 atom, and W10, W13, W4 and OH3 form part of the coordination structure of the copper Cu2 atom. Thus, W4 connects the coordination polyhedra of the two copper atoms. Water molecule W7 does not belong to the coordination structure of any atom and, therefore, is a free water molecule. As has been said, OH3 forms part of the coordination sphere of Cu2 atom. The hydrogen bond structure derived from the computations is displayed in Figure 6. As can be observed in Figure 6 and Table 3, there are thirteen non-equivalent hydrogen bonds. In the first hydrogen bond, OW1–H1WA· · ·OW16, the donor oxygen atom, OW1, is from a W1 water molecule (belonging to Cu1 coordination structure), and the acceptor oxygen atom, O16, belongs to a S-coordination polyhedron. The second H bond is from W1, and the acceptor O atom is from OH3, belonging to Cu2 coordination environment. The hydrogen bonds from OW4 link Cu1 polyhedra with O atoms from S tetrahedra (O15) and a free water molecule (W7). The hydrogen bonds from free water molecule W7 include one with water molecule OW10 from the Cu2 coordination structure, while the other links W7 with an O atom (O6) of the U1 coordination polyhedra. The hydrogen bonds from W9 link Cu1 with O8 and O11 from U1 and U2. The hydrogen bonds from OW10 link Cu2 with O6 and O14 from U1 and U2. The hydrogen bonds from W13 link Cu2 with O8 from U1 and with the free water molecule W7. Finally, OH3 links Cu2 polyhedra with O17 from U2. Consequently, the hydrogen bond structure in pseudojohannite serves to hold the full structure together by linking: (1) Cu octahedra, S tetrahedra and U bipyramids and (2) Cu octahedra and U bipyramids with free water.
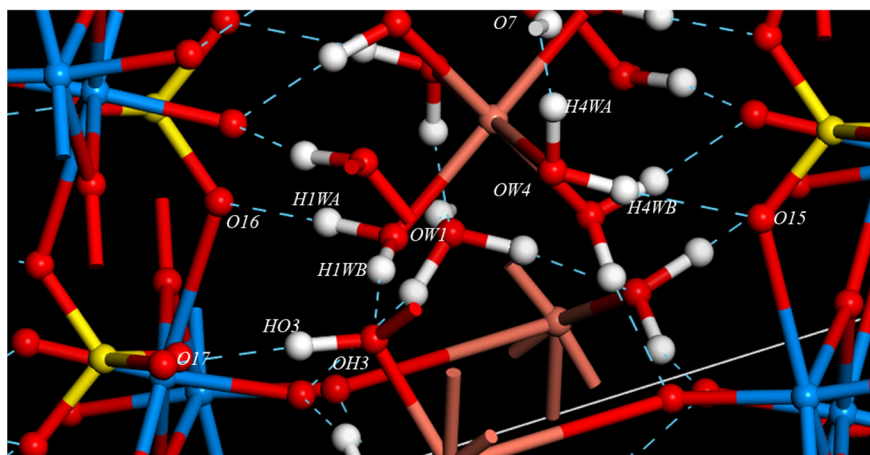
Figure 6. Hydrogen bonding structure in the crystal structure of pseudojohannite. Hydrogen bonds donated by OW1 and OW4 and OH3.

Table 3. Hydrogen bond parameters in pseudojohannite (distances are given in Å and angles in degrees).

Hydrogen bond O1-H···O2	O1···O2	H···O2	α (O1-H···O2)
	OW-H···O		
OW1-H1WA···O16	2.805	1.837	167.15
OW1-H1WB···OH3	2.601	1.598	168.62
OW4-H4WA···OW7	2.736	1.754	169.12
OW4-H4WB···O15	2.946	1.999	162.49
OW7-H7WA···O6	3.029	2.400	157.18
OW7-H7WB···OW10	2.955	2.196	133.82
OW9-HW9A···O11	2.904	1.928	171.65
OW9-HW9B···O8	2.699	1.712	172.23
OW10-HW10A···O6	2.802	1.928	146.71
OW10-HW10B···O14	2.662	1.664	174.05
OW13-HW13A···O8	2.776	1.834	158.62
OW13-HW13B···OW7	2.751	1.807	156.94
	OH-H···O		
OH3-HO3···O17	2.797	1.811	175.00

3.1.3. Derriksite

The crystal structure of derriksite is displayed in Figure 7. There is one non-equivalent uranium atom and three and two nonequivalent copper and selenium atoms in the derriksite unit cell. Uranium atoms in derriksite display tetragonal bipyramidal coordination and copper atoms display octahedral coordination. Selenium atoms are arranged in the form of trigonal pyramids, SeO_3, where the upper apex is occupied by the selenium atom (Figure 3). The crystal structure of derriksite is constructed from one-dimensional uranyl selenite chains directed along the [1 0 0] crystallographic direction. In between two uranyl selenite chains, the copper octahedral layers are arranged parallel to the (110) plane, in which each Cu atom has four OH groups shared with the neighboring Cu atoms. The chains and octahedral layers are linked through selenite coordination polyhedra as displayed in Figure 3. Two subsequent uranyl polyhedra in a given uranyl selenite chain are linked by sharing adjacent vertices with selenite groups. The oxygen atoms in the two opposed SeO_3 pyramids are disposed up and down relative to the plane of the chain of the U bipyramids. The stereochemically active lone-electron pair in Se atom is thus disposed down or up of the chain plane. In a given uranyl selenite chain the selenite lone pairs are always disposed in the same way, for example, (ud)-(ud) . . . , and in the next chain (to the right in Figure 7A) they take the opposite form, (du)-(du). Therefore, in a selenite group, two of the oxygen

triangle vertices connect two uranyl bipyramids and the remaining one link uranyl selenite chains and copper layers.
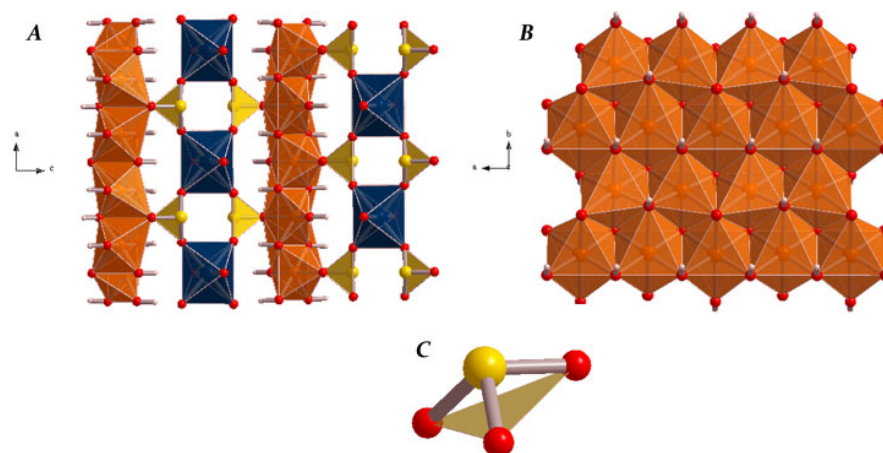

Figure 7. Structure of mineral derriksite: (**A**) view of the full unit cell from [0 1 0]; (**B**) copper octahedral layer; (**C**) selenium trigonal pyramids. Color code: U—blue; Cu—orange; Se—yellow; O—red; H—white.

The computed lattice parameters of derriksite, given in Table 1, have larger differences with respect to experiment than those of johannite and pseudojohannite. The unit cell volume is overestimated by 5.5%. The overestimation of the unit cell volume obtained using the PBE functional without dispersion corrections is 9.9%. The most probable reason for the larger differences in the computed unit cell parameters with respect to their experimental counterparts in derriksite compared to in johannite and pseudojohannite is the inferior quality and transferability of the norm-conserving pseudopotential employed to describe the inner electrons of selenium atom in derriksite. The calculated interatomic distances agree well with the experimental ones [27], as can be appreciated in Table S7 of the SM. The X-ray diffraction patterns derived from the calculated and experimental crystal structures, given in Figure 1 and Table S10, are also in good agreement.

Hydrogen Bonding Network

There are four non-equivalent hydroxyl ions in derriksite, OH1, OH2, OH3 and OH4. All of them belong to the copper coordination structure. The hydrogen bonds in derriksite are given in Table 4 and shown in Figure 8. There are four types of hydrogen bonds in derriksite: OH2-HO2···O9, OH3-HO3···O9, OH4-HO4···O1 and OH5-HO5···O8. In the first and second hydrogen bonds, the donor atoms are the hydroxyl oxygen atoms HO2 and HO3, forming part of copper coordination octahedra, and the acceptor oxygen ion is O9 from a selenite group. Thus, the O9 atom receives two hydrogen bonds donated by the hydroxyl oxygen atoms OH2 and OH3. The third and fourth hydrogen bonds are donated by OH4 and OH5 from Cu octahedra and are received by O1 and O8 from U1 bipyramids. Thus, the hydrogen bond structure in derriksite serves to link Cu octahedra with Se and U polyhedra.

Table 4. Hydrogen bond parameters in derriksite (distances are given in Å and angles in degrees).

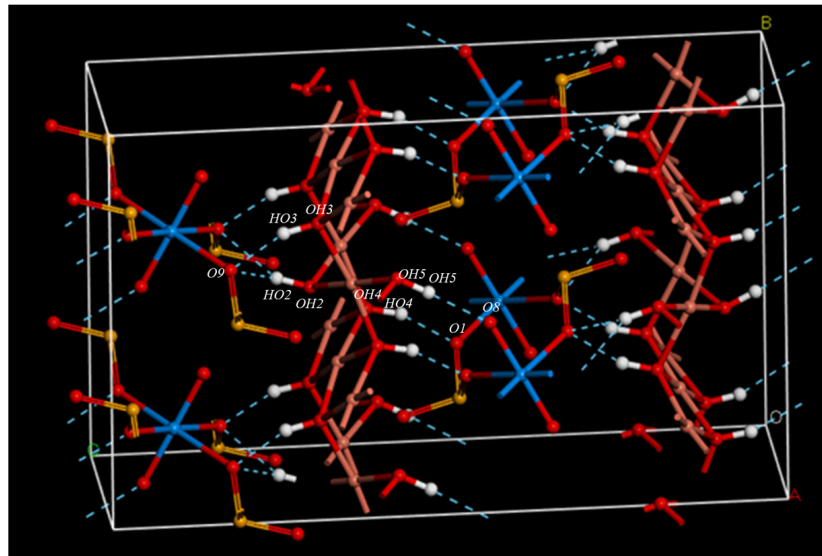| Hydrogen Bond	Exp. (This Work)			Calc.		
	O1···O2	H···O2	α(O1-H···O2)	O1···O2	H···O2	α(O1-H···O2)
OH2-HO2···O9	3.144	2.399	135.87	3.174	2.425	133.45
OH3-HO3···O9	2.839	2.046	139.79	2.757	1.803	159.93
OH4-HO4···O1	2.820	1.883	170.66	2.719	1.759	160.68
OH5-HO5···O8	3.091	2.173	161.53	2.938	1.957	177.37

Figure 8. Hydrogen bonding structure in the crystal structure of derriksite.

3.2. Mechanical Properties

3.2.1. Elastic Constants and Mechanical Stability

The computed elastic tensors of johannite, pseudojohannite and derriksite are given in Table 5. Since johannite and pseudojohannite are triclinic, all the elastic constants are non-vanishing. However, derriksite is monoclinic and has only nine non-vanishing elastic constants. The general Born mechanical stability condition is that the elastic matrices of these minerals should be positive definite, that is, all their eigenvalues are non-vanishing [67,68]. Therefore, all these tensors were diagonalized using numerical methods. Since all the computed eigenvalues were positive, it follows that the structures of the three minerals are mechanically stable.

Table 5. Computed elastic constants of johannite and pseudojohannite. All the values are given in GPa.

ij	C_{ij}		
	Johannite	**Pseudojohannite**	**Derriksite**
11	36.85	99.90	110.55
22	82.02	97.70	45.29
33	24.97	56.62	63.19
44	23.43	14.72	10.97
55	7.19	21.02	9.44
66	8.67	28.99	21.78
12	8.42	41.27	24.48
13	8.42	31.41	29.23
14	2.59	0.29	0.0
15	3.71	14.56	0.0
16	5.33	−5.64	0.0
23	82.02	17.12	16.13
24	6.08	15.67	0.0
25	3.10	6.72	0.0
26	−0.64	−5.92	0.0
34	7.13	0.80	0.0
35	4.04	−7.05	0.0
36	6.38	0.66	0.0
45	−0.59	5.53	0.0
46	2.24	5.38	0.0
56	1.38	0.69	0.0

3.2.2. Mechanical Properties

The elastic properties for polycrystalline aggregates of these minerals were obtained in terms of the calculated elastic constants, using the Reuss [69], Voigt [70] and Hill [71] approaches. The best approximation, defined as that giving the best approximation of the bulk modulus to the bulk modulus obtained from the 4-BM EOS, was found to be, as in many previous cases [39,41,42,57–61], the Reuss approximation. The computed mechanical properties obtained using this approximation are given in Table 6. The mechanical properties of mineral uranopilite, determined in a previous work [5], are also included in the table for comparison. While uranopilite and johannite have a low bulk modulus of the order of $B \sim 20$ GPa and, therefore, are quite compressible (compressibility is the inverse of bulk modulus), pseudojohannite and derriksite have larger bulk modulus. Similarly, uranopilite and johannite are less shear-resistant than pseudojohannite and derriksite in accordance with the values of the shear moduli, G. As can be seen, as uranopilite, the three minerals are ductile because the computed ductility index [72] is larger than 1.75 [73]. Furthermore, the three minerals are weak, because the Vickers hardness [74] is small. Reference values of the Vickers hardness (H), measuring the resistance of a material to indentation, may be found in a previous paper [61]. Finally, while johannite and pseudojohannite are quite mechanically anisotropic, their universal anisotropy index, A^U [75], is much smaller than that of uranopilite (A^U values are 3.28 and 3.19, respectively, in johannite and pseudojohannite). Derriksite is quite isotropic ($A^U = 1.36$). The dependence of the mechanical properties of johannite, pseudojohannite and derriksite are displayed in Figure 9. As can be seen, no mechanical anomalies, easily detected by analyzing these graphs [57–61], are present in these minerals. The presence of mechanical anomalies, such as the negative linear compressibility [76] and the negative Poisson's ratio [77], is usually correlated with the mechanical anisotropy [57–62]. The fact that the universal anisotropy index of uranopilite is almost double than in johannite and pseudojohannite is in accordance with the presence of negative mechanical phenomena in the first and the absence of them in the latter ones.

Table 6. Calculated mechanical properties of uranopilite, johannite, pseudojohannite and derriksite in the Reuss approximation. The values of the bulk, Young's and shear moduli (B, G and E) are given in GPa units. The computed bulk modulus and its first two derivatives with respect to pressure derived from the 4-BM-EOS are also given.

	Property	Uranopilite	Johannite	Pseudojohannite	Derriksite
	Elastic constants				
B	Bulk modulus	21.52 ± 1.33	20.90 ± 0.62	39.34 ± 0.51	33.47 ± 1.06
G	Shear modulus	10.94	11.57	15.01	14.91
E	Young's modulus	28.06	29.30	39.95	38.95
ν	Poisson's ratio	0.28	0.27	0.33	0.31
D	Ductility index	1.97	1.81	2.62	2.24
H	Hardness index	0.67	1.19	0.22	0.77
A^U	Universal anisotropy	6.65	3.28	3.19	1.36
	4-BM-EOS				
B (GPa)	Bulk modulus	20.74 ± 0.44	21.97 ± 0.42	41.97 ± 0.77	33.06 ± 0.29
B'	Bulk modulus first derivative	7.30 ± 0.58	2.56 ± 0.66	2.27 ± 1.07	12.05 ± 0.46
B'' (GPa^{-1})	Bulk modulus second derivative	-2.21 ± 0.50	1.87 ± 0.43	0.75 ± 0.56	-6.30 ± 0.60
χ^2	χ^2 parameter (fit)	0.004	0.002	0.002	0.001

A. JOHANNITE

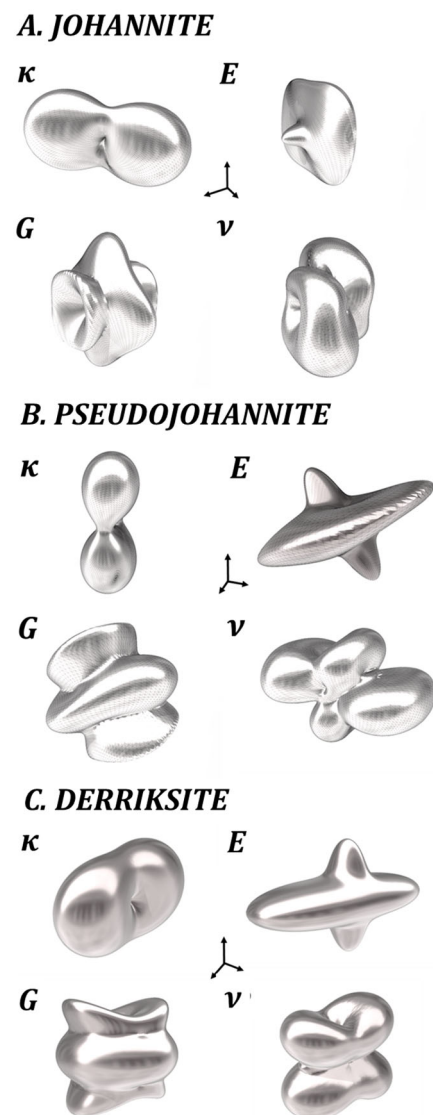## B. PSEUDOJOHANNITE

C. DERRIKSITE

Figure 9. Elastic properties of (**A**) johannite, (**B**) pseudojohannite and (**C**) derriksite minerals as a function of the orientation of the applied strain: (κ) Compressibility; (E) Young's modulus; (G) Shear modulus; (ν) Poisson's ratio. The largest values of the compressibility, Young's modulus, shear modulus and Poisson's ratio are 36.42 TPa^{-1}, 45.35 GPa, 27.59 GPa and 0.87 for johannite, 19.98 TPa^{-1}, 91.59 GPa, 35.37 GPa and 0.93, for pseudojohannite, and 17.03 TPa^{-1}, 31.06 GPa, 26.39 GPa and 0.66 for derriksite, respectively.

4. Conclusions

The complete crystal structures of johannite, pseudojohannite and derriksite, containing the positions of the hydrogen bonds, were determined by employing first principles theoretical methods based on periodic density functional theory employing basis sets composed from plane-waves and norm-conserving pseudopotentials. The calculated unit cell parameters, interatomic distances and X-ray powder patterns were in very good agreement with the experimental information. For derriksite, the crystal structure was also determined by refinement from X-ray diffraction data, with the resulting structure being consistent with the structure determined theoretically. The availability of these crystal structures made it possible to theoretically determine its elastic tensor and equation of state, because knowledge of optimized complete crystal structures is required for the application of first principles methods. The mechanical stability of johannite, pseudojohannite and derriksite, and a rich set of important mechanical properties were derived from the calculated elasticity matrix and equation of state. The values of the bulk, Young's and shear moduli,

the Poisson's ratio and the ductility, anisotropy and hardness indices, as well as the bulk modulus derivatives with respect to pressure were predicted since these properties have not been measured experimentally. The unit cells of johannite and pseudojohannite are highly hydrated, containing eight and twelve water molecules per formula unit. Thus, a large fraction of the atoms in their unit cells belongs to water molecules or hydroxyl ions (61 and 62%). The study of highly hydrated materials using theoretical methods is a great challenge due to the weak nature of the interactions between the water molecules themselves and with the remaining constituents in the unit cells. The excellent quality of the results obtained in this and previous works [5,39,41–43] for this kind of materials indicate that, indeed, *state of the art* first principles methodologies are capable of accurately describing the crystal structure and properties of highly hydrated materials.

The present results should be extended to study the vibrational spectra and thermodynamic properties of these minerals. The infrared and Raman spectra of these minerals are fundamental for their identification, and their computation using first principles methods must allow for their rigorous assignment, as shown in previous works [5,41,42]. Furthermore, the knowledge of their thermodynamic functions is crucial for studying their formation processes and understanding the paragenetic sequence of these minerals arising due to the oxidation/hydration processes occurring in uranite deposits and spent fuel nuclear waste repositories. Their Gibbs free energies and entropies determine fundamental parameters, such as solubility and reaction constants [40,78,79], that are required for the simulation of the migration of uranium from uraninite deposits, nuclear waste repositories, and uranium-contaminated sites. The knowledge base acquired in previous studies [40,78,79] should allow for the study of the relative thermodynamic stability of these minerals relative to a wide series of secondary phases of nuclear fuel as a function of temperature.

References

1. Alcorn, C.D.; Cox, J.S.; Lucas, M.S.G.A.; Tremaine, P.R. Investigation of Uranyl Sulfate Complexation under Hydrothermal Conditions by Quantitative Raman Spectroscopy and Density Functional Theory. *J. Phys. Chem. B* **2019**, *123*, 7385–7409. [CrossRef] [PubMed]
2. Cook, W.G.; Lister, D.H. Chemistry in CANDU Process Systems. In *The Essential CANDU: A Textbook on the CANDU Nuclear Power Plant Technology*; Garland, W.J., Ed.; University Network in Nuclear Engineering: Hamilton, ON, Canada, 2014.
3. Gelfort, E. Nutzung der spaltprodtikte nach aufarbeitung ausgedienter brennelemente. *Atw. Atomwirtsch. Atomtechnik.* **1985**, *30*, 32–36.
4. Chen, F.; Burns, P.C.; Ewing, R.C. [79]Se: Geochemical and crystallo-chemical retardation mechanisms. *J. Nucl. Mater.* **1999**, *275*, 81–88. [CrossRef]
5. Colmenero, F.; Plášil, J.; Timón, V.; Čejka, J. Full crystal structure, hydrogen bonding and spectroscopic, mechanical and thermodynamic properties of mineral uranopilite. *RSC Adv.* **2020**, *10*, 31947–31960. [CrossRef] [PubMed]
6. John, F.J. Chemische untersuchung eines natürlichen Uranvitriols. *Chem. Unters.* **1821**, *5*, 254–256.
7. Haidinger, W. Ober den Johannit, eine neue Spezies des Mineralreiches. *Ann. Phys. Berl. Ger.* **1830**, *3*, 305–310.
8. Haidinger, W. On johannite, a new mineral species. *Edinb. J. Sci.* **1830**, *3*, 306–310.
9. Larsen, E.S.; Berman, H. The identity of gilpinite and johannite. *Am. Min.* **1926**, *11*, 1–5.
10. Nováček, R. Study on some secondary uranium minerals. *Věstník Královské České Společnosti. Nauk.* **1935**, *7*, 1–36.
11. Peacock, M.A. On Johannite from Joachimsthal and Colorado. *Z. Kristallogr.* **1935**, *90*, 112–119. [CrossRef]
12. Hurlbut, C.S. Studies of uranium minerals (IV): Johannite. *Am. Mineral.* **1950**, *35*, 531–535.
13. Donnay, J.D.H. The primitive cell of johannite. *Am. Mineral.* **1955**, *40*, 1131–1132.
14. Appleman, D.E. Crystal chemical study of johannite. *Bull. Geol. Soc. Amer. Abstr.* **1957**, *68*, 1696.
15. Mereiter, K. Die Kristallstruktur des Johannits. *Fortschr. Min.* **1981**, *59*, 125.
16. Mereiter, K. Die kristallstruktur des Johannits, $Cu(UO_2)_2(SO_4)_2(OH)_2 \cdot 8H_2O$. *Tschermaks Min. Petr. Mitt.* **1982**, *30*, 47–57. [CrossRef]
17. Čejka, J.; Urbanec, Z. Thermal and Infrared Spectrum Analyses of Johannite. In Proceedings of the Second European Symposium on Thermal Analysis, Aberdeen, UK, 1–4 September 1981; pp. 520–524.
18. Čejka, J.; Urbanec, Z.; Čejka, J.; Mrázek, Z. Contribution to the thermal analysis and crystal chemistry of johannite $Cu(UO_2)_2(SO_4)_2(OH)_2 \cdot 8H_2O$. *Neues Jahrb. Mineral. Abh.* **1988**, *153*, 297–309.
19. Sokol, F.; Čejka, J. A thermal and mass spectrometric study of synthetic johannite $Cu(UO_2)_2(SO_4)_2(OH)_2 \cdot 8H_2O$. *Thermochim. Acta* **1992**, *206*, 235–242. [CrossRef]
20. Frost, R.L.; Erickson, K.L.; Čejka, J.; Reddy, B.J. A Raman spectroscopic study of the uranyl sulphate mineral johannite. *Spectrochim. A* **2005**, *61*, 2702–2707. [CrossRef] [PubMed]
21. Ondruš, P.; Veselovský, F.; Skála, R.; Císařová, I.; Hloušek, J.; Frýda, J.; Vavřín, I.; Čejka, J.; Gabašová, A. New naturally occurring phases of secondary origin from Jáchymov (Joachimsthal). *J. Czech Geol. Soc.* **1997**, *42*, 77–107.
22. Ondruš, P.; Veselovský, F.; Gabašová, A.; Hloušek, J.; Šrein, V. Supplement to secondary and rock-forming minerals of the Jáchymov ore district. *J. Czech Geol. Soc.* **2003**, *48*, 149–155.
23. Brugger, J.; Wallwork, K.S.; Meisser, N.; Pring, A.; Ondruš, P.; Čejka, J. Pseudojohannite from Jáchymov. Musonoï, and La Creusaz: A new member of the zippeite group. *Am. Min.* **2006**, *91*, 929–936. [CrossRef]
24. Plášil, J.; Fejfarová, K.; Wallwork, K.S.; Dušek, M.; Škoda, R.; Sejkora, J.; Čejkam, J.; Veselovský, F.; Hloušek, J.; Meisser, N.; et al. Crystal structure of pseudojohannite, with a revised formula, $Cu_3(OH)_2[(UO_2)_4O_4(SO_4)_2](H_2O)_{12}$. *Amer. Mineral.* **2012**, *97*, 1796–1803. [CrossRef]
25. Plášil, J. Crystal structure refinement of pseudojohannite, $Cu_3(OH)_2[(UO_2)_4O_4(SO_4)_2](H_2O)_{12}$, from the type locality—Jáchymov, Czech Republic. *J. Geosci.* **2015**, *60*, 123–127. [CrossRef]
26. Cesbron, F.; Pierrot, R.; Verbeek, T. La derriksite, $Cu_4(UO_2)(SeO_3)_2(OH)_6 \cdot H_2O$, une nouvelle espèce minérale. *Bull. Soc. Fr. Minéral. Cristallogr.* **1971**, *94*, 534–537.
27. Ginderow, D.; Cesbron, F. Structure da la derriksite, $Cu_4(UO_2)(SeO_3)_2(OH)_6$. *Acta Crystallogr. C* **1983**, *39*, 1605–1607. [CrossRef]
28. Frost, R.L.; Reddy, B.J.; Dickfos, M.J. An application of near infrared and mid-infrared spectroscopy to the study of uranyl selenite minerals: Derriksite, demesmaekerite, guilleminite and haynesite. *J. Near Infrared Spectrosc.* **2008**, *16*, 455–469. [CrossRef]
29. Frost, R.L.; Čejka, J.; Scholz, R.; Lopez, A.; Theiss, F.L.; Xi, Y. Vibrational spectroscopic study of the uranyl selenite mineral derriksite $Cu_4(UO_2)(SeO_3)_2(OH)_6 \cdot H_2O$. *Spectrochim. Acta A* **2014**, *117*, 473–477. [CrossRef] [PubMed]
30. Gurzhiy, V.V.; Kuporev, I.V.; Kovrugin, V.M.; Murashko, M.N.; Kasatkin, A.V.; Plášil, J. From Crystal Chemistry and Structural Complexity of Natural and Synthetic Uranyl Selenites. *Crystals* **2019**, *9*, 639. [CrossRef]
31. Gurzhiy, V.V.; Izatulina, A.R.; Krzhizhanovskaya, M.G.; Murashko, M.N.; Spiridonova, D.V.; Shilovskikh, V.V.; Krivovichev, S.V. Thermal behavior of uranyl selenite minerals derriksite and demesmaekerite. *J. Geosci.* **2020**, *65*, 249–259. [CrossRef]
32. Krivovichev, S.V.; Plášil, J. Mineralogy and crystallography of uranium. In *Uranium: From Cradle to Grave*; Burns, P.C., Sigmon, G.E., Eds.; Mineralogical Association of Canada, Short Courses 43: Québec City, QC, Canada, 2013; pp. 15–119.
33. Plášil, J. Oxidation–hydration weathering of uraninite: The current state-of-knowledge. *J. Geosci.* **2014**, *59*, 99–114. [CrossRef]
34. Baker, R.J. Uranium minerals and their relevance to long term storage of nuclear fuels. *Coord. Chem. Rev.* **2014**, *266–267*, 123–136. [CrossRef]

35. Nordstrom, D.K.; Alpers, C.N. Geochemistry of acid mine waters. In *Reviews in Economic Geology*; Plumlee, G.S., Logsdon, M.J., Eds.; Society of Economic Geologists: Littleton, CO, USA, 1999; Volume 6A, Ch. 6; pp. 133–160.

36. Edwards, K.J.; Bond, P.L.; Druschel, G.K.; Mcguire, M.M.; Hamers, R.J.; Banfield, J.F. Geochemical and biological aspects of sulfide mineral dissolution: Lessons from Iron Mountain, California. *Chem. Geol.* **2000**, *169*, 383–397. [CrossRef]

37. Bian, Z.; Miao, X.; Lei, S.; Chen, S.; Wang, W.; Struthers, S. The challenges of reusing mining and mineral-processing wastes. *Science* **2002**, *37*, 702–703. [CrossRef] [PubMed]

38. Jamieson, H.E.; Walke, S.R.; Parsons, M.B. Mineralogical Characterization of Mine Waste. *Appl. Geochem.* **2015**, *57*, 85–105. [CrossRef]

39. Colmenero, F.; Plášil, J.; Sejkora, J. The crystal structures and mechanical properties of the uranyl carbonate minerals roubaultite, fontanite, sharpite, widenmannite, grimselite and čejkaite. *Inorg. Chem. Front.* **2020**, *7*, 4197–4221. [CrossRef]

40. Colmenero, F. Thermodynamic properties of the uranyl carbonate minerals roubaultite, fontanite, widenmannite, grimselite, čejkaite and bayleyite. *Inorg. Chem. Front.* **2020**, *7*, 4160–4179. [CrossRef]

41. Colmenero, F.; Cobos, J.; Timón, V. Periodic Density Functional Theory Study of the Structure, Raman Spectrum, and Mechanical Properties of Schoepite Mineral. *Inorg. Chem.* **2018**, *57*, 4470–4481. [CrossRef]

42. Colmenero, F.; Plášil, J.; Sejkora, J. The layered uranyl silicate mineral uranophane-β: Crystal structure, mechanical properties, Raman spectrum and comparison with the α-polymorph. *Dalton Trans.* **2018**, *48*, 16722–16736. [CrossRef] [PubMed]

43. Oxford Diffraction Ltd. *Rigaku Oxford Diffraction: CrysAlisCCD, CrysAlisRED and CrysAlis PRO*; Oxford Diffraction Ltd.: Oxfordshire, UK, 2019.

44. Sheldrick, G.M. SHELXT—Integrated Space-Group and Crystal-Structure Determination. *Acta Crystallogr.* **2015**, *71*, 3–8. [CrossRef] [PubMed]

45. Crystallographic Computing System for Standard and Modulated Structures. 2006. Available online: https://jana.fzu.cz/ (accessed on 19 September 2019).

46. Payne, M.C.; Teter, M.P.; Ailan, D.C.; Arias, A.; Joannopoulos, J.D. Iterative Minimization Techniques for ab Initio Total-Energy Calculations: Molecular Dynamics and Conjugate Gradients. *Rev. Mod. Phys.* **1992**, *64*, 1045–1097. [CrossRef]

47. Clark, S.J.; Segall, M.D.; Pickard, C.J.; Hasnip, P.J.; Probert, M.I.J.; Refson, K.; Payne, M.C. First principles methods using CASTEP. *Z. Kristallogr.* **2005**, *220*, 567–570. [CrossRef]

48. MaterialsStudio. Available online: https://3dsbiovia.com/products/collabo-rative-science/biovia-materials-studio/ (accessed on 15 June 2022).

49. Perdew, J.P.; Burke, K.; Ernzerhof, M. Generalized Gradient Approximation Made Simple. *Phys. Rev. Lett.* **1996**, *77*, 3865–3868. [CrossRef] [PubMed]

50. Grimme, S. Semiempirical GGA-type Density Functional Constructed with a Long-Range Dispersion Correction. *J. Comput. Chem.* **2006**, *27*, 1787–1799. [CrossRef] [PubMed]

51. Troullier, N.; Martins, J.L. Efficient Pseudopotentials for Plane-Wave Calculations. *Phys. Rev. B* **1991**, *43*, 1993–2006. [CrossRef] [PubMed]

52. Bonales, L.J.; Colmenero, F.; Cobos, J.; Timón, V. Spectroscopic Raman characterization of rutherfordine: A combined DFT and experimental study. *Phys. Chem. Chem. Phys.* **2016**, *18*, 16575–16584. [CrossRef] [PubMed]

53. Pfrommer, B.G.; Cote, M.; Louie, S.G.; Cohen, M.L. Relaxation of Crystals with the Quasi-Newton Method. *J. Comput. Phys.* **1997**, *131*, 233–240. [CrossRef]

54. Downs, R.T.; Bartelmehs, K.L.; Gibbs, G.V.; Boisen, M.B. Interactive software for calculating and displaying X-ray or neutron powder diffractometer patterns of crystalline materials. *Am. Mineral.* **1993**, *78*, 1104–1107.

55. Nye, J.F. *Physical Properties of Crystals*; Clarendon: Oxford, UK, 1976.

56. Yu, R.; Zhu, J.; Ye, H.Q. Calculations of Single-Crystal Elastic Constants Made Simple. *Comput. Phys. Commun.* **2010**, *181*, 671–675. [CrossRef]

57. Colmenero, F. Mechanical properties of anhydrous oxalic acid and oxalic acid dihydrate. *Phys. Chem. Chem. Phys.* **2019**, *21*, 2673–2690. [CrossRef] [PubMed]

58. Colmenero, F. Organic acids under pressure: Elastic properties, negative mechanical phenomena and pressure induced phase transitions in the lactic, maleic, succinic and citric acids. *Mater. Adv.* **2020**, *1*, 1399–1426. [CrossRef]

59. Colmenero, F. Silver Oxalate: Mechanical Properties and Extreme Negative Mechanical Phenomena. *Adv. Theor. Simul.* **2019**, *2*, 1900040. [CrossRef]

60. Colmenero, F.; Jiang, X.; Li, X.; Li, Y.; Lin, Z. Negative area compressibility in silver oxalate. *J. Mater. Sci.* **2021**, *56*, 269–277. [CrossRef]

61. Colmenero, F. Negative Linear Compressibility in Nanoporous Metal–Organic Frameworks Rationalized by the Empty Channel Structural Mechanism. *Phys. Chem. Chem. Phys.* **2021**, *23*, 8508–8524. [CrossRef] [PubMed]

62. Marmier, A.; Lethbridge, Z.A.D.; Walton, R.I.; Smith, C.; Parker, S.C.; Evans, K.E. ElAM: A computer program for the analysis and representation of anisotropic elastic properties. *Comput. Phys. Commun.* **2010**, *181*, 2102–2115. [CrossRef]

63. Birch, F. Finite Elastic Strain of Cubic Crystals. *Phys. Rev.* **1947**, *71*, 809–824. [CrossRef]

64. Angel, R.J. Equations of State. *Rev. Mineral. Geochem.* **2000**, *41*, 35–49. [CrossRef]

65. EOSFIT 5.2 Software. Available online: http://programming.ccp14.ac.uk/ccp/web-mirrors/ross-angel/crystal/software.html (accessed on 15 September 2020).

66. Burns, P.C.; Hawthorne, F.C. Coordination geometry structural pathways in Cu^{2+} oxysalt minerals. *Can. Mineral.* **1995**, *33*, 889–905.

67. Born, M. On the Stability of Crystal Lattices. I. *Math. Proc. Camb. Philos. Soc.* **1940**, *36*, 160–172. [CrossRef]

68. Mouhat, F.; Coudert, F.X. Necessary and sufficient elastic stability conditions in various crystal systems. *Phys. Rev. B* **2014**, *90*, 224104. [CrossRef]

69. Voigt, W. *Lehrbuch der Kristallphysik*; Teubner: Leipzig, Germany, 1962.

70. Reuss, A. Berechnung der Fliessgrenze von Mischkristallen auf Grund der Plastizitatsbedingung fur Einkristalle. *Z. Angew. Math. Mech.* **1929**, *9*, 49–58. [CrossRef]

71. Hill, R. The Elastic Behaviour of a Crystalline Aggregate. *Proc. Phys. Soc. Lond. A* **1952**, *65*, 349–354. [CrossRef]

72. Pugh, S.F. XCII. Relations between the Elastic Moduli and the Plastic Properties of Polycrystalline Pure Metals. *Phil. Philos. Mag.* **1954**, *45*, 823–843. [CrossRef]

73. Bouhadda, Y.; Djella, S.; Bououdina, M.; Fenineche, N.; Boudouma, Y. Structural and Elastic Properties of LiH_4 for Hydrogen. Storage Applications. *J. Alloys. Compd.* **2012**, *534*, 20–24. [CrossRef]

74. Niu, H.; Wei, P.; Sun, Y.; Chen, C.X.; Franchini, C.; Li, D.; Li, Y. Electronic, Optical, and Mechanical Properties of Superhard Cold-Compressed Phases of Carbon. *Appl. Phys. Lett.* **2011**, *99*, 031901. [CrossRef]

75. Ranganathan, S.I.; Ostoja-Starzewski, M. Universal Elastic Anisotropy Index. *Phys. Rev. Lett.* **2008**, *101*, 055504. [CrossRef]

76. Cairns, A.B.; Goodwin, A.L. Negative linear compressibility. *Phys. Chem. Chem. Phys.* **2015**, *17*, 20449–20465. [CrossRef] [PubMed]

77. Lakes, R.S. Negative-Poisson's-Ratio Materials: Auxetic Solids. *Annu. Rev. Mater. Res.* **2017**, *47*, 63–81. [CrossRef]

78. Colmenero, F.; Fernández, A.M.; Cobos, J.; Timón, V. Thermodynamic Properties of Uranyl-Containing Materials Based on Density Functional Theory. *J. Phys. Chem. C* **2018**, *122*, 5254–5267. [CrossRef]

79. Colmenero, F.; Fernández, A.M.; Cobos, J.; Timón, V. Temperature-Dependent Gibbs Free Energies of Reaction of Uranyl-Containing Materials Based on Density Functional Theory. *J. Phys. Chem. C* **2018**, *122*, 5268–5279. [CrossRef]